Published in final edited form as:

Clin Cancer Res. 2018 December 01; 24(23): 5977–5989. doi:10.1158/1078-0432.CCR-18-0269.

Therapeutic targeting of TFE3/IRS-1/PI3K/mTOR axis in translocation renal cell carcinoma

Nur P. Damayanti[1], **Justin A. Budka**[2], **Heba W.Z Khella**[3], **Mary W. Ferris**[2], **Sheng Yu Ku**[4], **Eric Kauffman**[5], **Anthony C. Wood**[1], **Khunsha Ahmed**[1], **Venkata Nithinsai Chintala**[1], **Remi Adelaiye-Ogala**[1], **May Elbanna**[1], **Ashley Orillion**[1], **Sreenivasulu Chintala**[1], **Chinghai Kao**[1], **W. Marston Linehan**[6], **George M Yousef**[3], **Peter C. Hollenhorst**[2], and **Roberto Pili**[1,*]

[1]Genitourinary Program, Division of Hematology & Oncology, Indiana University Melvin and Bren Simon Cancer Center; [2]Medical Sciences, Indiana University School of Medicine, Bloomington, Indiana; [3]Department of Laboratory Medicine and the Keenan Research Centre for Biomedical Science at the Li KaShing Knowledge Institute, St. Michael's Hospital, Toronto, Canada, [4]Department of Pharmacology & Therapeutics and [5]Department of Urology and Department of Cancer Genetics Roswell Park Cancer Institute, Buffalo, NY 14263, USA, [6]Urologic Oncology Branch, National Cancer Institute, National Institutes of Health, Bethesda MD 20892

Abstract

Purpose: Translocation renal cell carcinoma (tRCC) represents a rare subtype of kidney cancer associated with various *TFE3, TFEB, or MITF* gene fusions that is not responsive to standard treatments for RCC. Therefore, the identification of new therapeutic targets represents an unmet need for this disease.

Experiment design: We have established and characterized a tRCC patient-derived xenograft (PDX), RP-R07, as a novel preclinical model for drug development by using next generation sequencing and bioinformatics analysis.We then assessed the therapeutic potential of inhibiting the identified pathway using *in vitro* and *in vivo* models.

Results: The presence of a *SFPQ-TFE3* fusion (t(X;1) (p11.2; p34)) with chromosomal break-points was identified by RNA-seq and validated by RT-PCR. TFE3 chromatin immunoprecipitation followed by deep sequencing (ChIP-Seq) analysis indicated a strong enrichment for the PI3K/AKT/mTOR pathway. Consistently, microRNA microarray analysis also identified PI3K/AKT/mTOR as a highly enriched pathway in RP-R07. Upregulation of PI3/AKT/mTOR pathway in additional TFE3-tRCC models were confirmed by significantly higher expression of phospho-S6 ($P<0.0001$) and phospho-4EBP1 ($P<0.0001$) in established tRCC cell lines compared to clear cell RCC cells. Simultaneous vertical targeting of both PI3K/AKT and mTOR axis provided a greater anti-proliferative effect both *in vitro* ($P<0.0001$) and *in vivo* ($P<0.01$) compared to single node inhibition. Knockdown of *TFE3* in RP-R07 resulted in decreased expression of IRS-1 and inhibited cell proliferation.

[*]**Corresponding author:**Roberto Pili, MD, Genitourinary Program, Indiana University-Simon Cancer Center, Indianapolis, IN, rpili@iu.edu.

Conflict of interest: No conflict of interest

Conclusion—These results identify TFE3/IRS-1/PI3K/AKT/mTOR as a potential dysregulated pathway in TFE3-tRCC, and suggest a therapeutic potential of vertical inhibition of this axis by using a dual PI3K/mTOR inhibitor for TFE3-tRCC patients.

Keywords

translocation renal cell carcinoma; patient-derived xenograft; PI3K/mTOR pathway

INTRODUCTION

Micropthalmia transcription factor (MiT) family tRCC is a distinct subtype of kidney cancer characterized by gene fusions resulting from translocations involving *TFE3* (Xp11.2 locus (1) or *TFEB* (6p21 locus) (2) with various partner gene (3). Since its introduction as a separate clinical entity in the 2004 World Health Organization classification of renal tumors, tRCC has gained increasing recognition in clinical practice. It is estimated that 1/3 of pediatric RCCs, 15% of RCCs in patients ≤ 45 years of age (4), and up to 4% of adult RCCs overall may have MiT family translocations (5). However, despite the clinical burden that tRCC presents, there is a paucity of data regarding effective management (6).

Despite the identification of multiple TFE3 gene fusions in tRCC including *PSF-TFE3*, *NONO-TFE3*, *PRCC-TFE3*(7), *ASPL-TFE3*(8), *CLTC-TFE3*(9), and recent novel fusion *TFE3-DVL-2* (10) and *TFE3-RBM10*(11), the molecular mechanisms underpinning tRCC oncogenesis are not well understood (3). Moreover, the heterogeneity of the dysregulated signaling pathways resulting from the variety of TFE3 gene fusions, combined with the lack of drugs targeting the chimeric oncoproteins, poses additional challenges to establish effective treatments. Genetically engineered cell lines (12), as well mouse models (13), have been generated to study the biology of various tumors harboring TFE3 fusions. However, more researchers are turning to patient-derived xenograft (PDX) models, which maintain the fidelity of the original tumor, including genomic integrity, tumor heterogeneity, and potential therapeutic responsiveness (14). Therefore, a PDX model can provide a translatable representation of tRCC in the laboratory setting that allows improving our understanding of tumorigenesis and the real-world applicability of treatment options.

Identifying the target genes and DNA binding landscape of TFE3 is critical to characterize its functional role as a transcription factor in a complex gene regulatory network. To date, studies utilizing next generation sequencing (NGS) technology have reported TFE3 target genes and DNA binding profile in embryonic stem cells (15), mouse embryonic fibroblasts (16), and melanoma cells (17). However, to the best of our knowledge, the target genes and DNA binding profile of TFE3 in tRCC cells have not yet been reported. Chromatin immunoprecipitation followed by deep sequencing (ChIP-Seq), an application of next NGS, provides an efficient method for global profiling of DNA-binding proteins and identification of their target sites on a genome wide scale. Therefore, ChIP-Seq is a valuable tool that could be used to gain novel biological insight of TFE3 gene regulatory networks and oncogenic pathways in tRCC.

In addition to transcription factors, microRNAs (miRNA) also play an integral role in a tightly controlled genetic regulatory system. MiRNAs are short, non-coding RNA molecules

that post-transcriptionally target messenger RNA (mRNA) to modulate gene expression (18). In highly inter-connected network, both transcription factors and miRNA work to orchestrate cascade and/or combined regulatory functions to facilitate cellular physiology (19). Therefore, analysis of both the miRNA and transcription factor regulatory network are pertinent in the identification of key genomic elements and their associated pathways. Furthermore, dysregulated miRNAs have been frequently implicated in carcinogenesis (20). Thus, their expression profile is of particular importance in oncology to aid in biomarker selection (21), cancer classification, and molecular target identification (22).

In this study, we established a novel tRCC PDX preclinical model to serve as a platform for improving our understanding of this disease. We performed molecular characterization studies, including RNA-seq, ChIP-seq, miRNA expression profiling by RT-PCR, and immunodetection techniques. We applied the molecular signatures of our tRCC PDX model to generate hypothesis regarding potentially targetable pathways involved in oncogenesis using bioinformatic pathway analysis tools. We subsequently assessed the therapeutic potential of inhibiting an identified dysregulated pathway in tRCC using both *in vitro* and *in vivo* studies.

Materials and Methods

Methods patient derived xenograft RP-R07t generation.

The studies presented were conducted in accordance with the Declaration of Helsinki, and after approval by the RPCI Institutional Review Board and obtaining written consent from the subject. Non-necrotic areas of lymphoid metastatic nodule from a tRCC patient were sectioned into ~4 mm^3 pieces. Fragments of the tumor containing both malignant cells and supportive stromal components, were implanted subcutaneously into the flanks implanted subcutaneously into anaesthetized 5-week to 6-week-old female NSG mice (The Jackson Laboratory, USA). During the engraftment phase, tumors were allowed to establish and grow and then were harvested upon reaching a size of 1,500 mm^3. Harvested tumor was divided for three purposes: 1) patient derived cell line; 2) subsequent expansion through serial passaging in NSG mice: 3) biological assays for histological and molecular characterization of established PDX. The mice (P1 generation) were maintained under pathogen-free conditions and a 12-hour light/dark cycle. When P1 tumors reached an approximate size of 1800 mm^3, they were harvested, fragmented, and reimplanted into additional mice (P2 generation) while maintained as a live bank according to approved Institutional Animal Care and Use Committee protocols. When enough P2 reached a volume greater than 200 mm^3, the animals were divided into 4 groups (Vehicle, Rapamycin, MLN0128 and BEZ-235).

Patient derived cells RP-R07.

RP-R07 tumor pieces (~4 mm^2) were placed in a 6 wells culture plate and removed after being cultured for 24 hours in supplemented DMEM high glucose media (10% FBS; 1% penicillin/streptomycin). Adherent cells were a mixed population of tumor cells and fibroblasts. These cells were cultivated with feeder cells and supplemented with ROCK inhibitor until approximately 80% confluent. Serial passaging of these heterogeneous

cultures was performed, until a homogeneous monolayer of RP-R07 cells was present. RP-R07 cell were subsequently cultured in DMEM medium (Gibco) supplemented with 10% fetal bovine serum and 1% penicillin/streptomycin at 37°C, 5% CO2. The UOK109 and UOK146 cell lines were established by Dr. Linehan's laboratory at the NCI (3).

Fusion detection by RNA-seq.

The RNeasy mini kit (Qiagen) was used for the isolation of RNA according to the manufacturer's instructions. Site specific reverse transcription was performed with the reverse transcriptase Superscript III (Invitrogen) and five 3' primers spaced throughout the TFE3 transcript. Following reverse transcription and subsequent second strand synthesis, the sequencing library for fusion detection was generated using an Illumina TruSeq sample preparation protocol for single-end reads. Reads were aligned using TopHat with Bowtie1 and the fusion search option selected. Finally, tophat fusion post was used to identify putative fusion transcripts with a minimum of 3 supporting fusion reads.

Fusion validation by RT-PCR.

Total RNA was extracted by TRIzol (Invitrogen) according to manufactures instructions. Two microgram of RNA was used to perform cDNA synthesis by iScript cDNA synthesis kit (Bio-Rad) and then subjected to PCR reactions. To detect hybrid transcripts the resulting cDNA was subject to amplification with the *SFPQ* exon 7 primer 5′-CGTCAACGTGAGATGGAAGA-3′ (forward primer) and the exon 6 *TFE3* primer 5′-GCAGGAGTTGCTGACAGTGA-3′ (reverse primer) for *SFPQ-TFE3*, *PRCC* exon 1 primer, 5′-AGGAAAGAGCCCGTGAAGAT-3′ (forward primer) and TFE3 exon 6 primer, 5′-GTTCTCCAGATGGGTCTGC-3′ (reverse primer) to detect PRCC-TFE3 and NONO exon 9 primer, 5′-ATCAAGGAGGCTCGTGAGAA-3′ (forward primer) and TFE3 exon 6 primer, 5′-GTTCTCCAGATGGGTCTGC-3′ (reverse primer) to detect *NONO-TFE3*. In these analysis, all reverse transcribed samples gave an β-actin PCR product of the expected size. The amplification conditions were 93°C for 20 s, 58°C for 40 s and 72°C for 40 s for 35 cycles in a final volume of 25 μl. The products were separated by electrophoresis in agarose gels followed by staining with ethidium bromide.

ChIP-seq and analysis.

ChIP was performed as previously describe (23). Cells were crosslinked using 1% v/v Formaldehyde (Fisher Scientific) for 15 minutes before quenching with 2M glycine for 5 minutes. Cells were sonicated for 3 minutes (30 sec ON, 30 sec OFF) using a Diagenode Bioruptor Pico water bath sonicator. Following sonication, the lysate was rotated with the TFE3 antibody (P16: sc-5958, Santa Cruz, USA) for 4 hours at 4°C before subsequent washing and DNA isolation by phenol-chloroform. Library preparation was performed as previously describe (24). Reads were aligned to the genome with Bowtie before duplications and hg19 blacklisted reads were removed. Peak calling was performed using Macs v1.4.2, and following peak calling, nearest neighboring genes were determined using the Useq platform (http://useq.sourceforge.net/). Enriched motifs were determined using the MEME-ChIP software within the MEME Suite online package for all called TFE3 binding sites.

Total RNA extraction for miRNA expression screening.

Total RNA isolation was done using the miRNeasy Kit (Qiagen, Mississauga, Canada) according to the manufacture's protocol. RNA quality and concentration were determined spectrophotometrically (NanoDrop 1000 Spectrophotometer; NanoDrop Technologies Inc., Wilmington, Delaware). Samples optimal for analysis were stored at −80˚C.

miRNA expression screening by TaqMan Low Density Array Cards.

500 ng total RNA from each sample were reverse transcribed using a Megaplex Primer Pool Human Set A+B (Life Technologies) with a TaqMan® miRNA reverse-transcription kit as suggested by the manufacturer. cDNA samples of individual patients were analyzed by a TaqMan® low-density array human microRNA card set A+B. Relative expression was determined using the ΔΔCT method and expression values were normalized to small nuclear RNA, U6 snRNA, RNU48 and RNU44.

MTT cell proliferation assay.

RP-R07, UOK-109 and UOK-146 cells (3000 cells/well) were seeded in 96-well plates and incubated for 24 h at 37 °C and 5% CO_2. The following day, cells were treated with drugs with defined concentrations. All drugs for in-vitro study sunitinib (LC laboratories), USA), gemcitabine (LC laboratories), USA), doxorubicin (LC laboratories), USA), crizotinib (LC laboratories), USA), BKM-120 (Novartis, USA), MLN0128 (Millenium, USA) and NVP-BEZ235 (Novartis, USA) were dissolved in DMSO for the preparation of stock solutions (10mM). Cell viability was determined by measuring dehydrogenase activity. We changed the medium and applied 100 μL of serum-free medium with 25 μL of MTT (3-(4,5-dimethylthiazol-2-yl)-2,5-diphenyltetrazolium bromide) (5 mg/mL) to each well and incubated the cells for 4 h at 37 °C and 5% CO_2 to allow the formation of a purple formazan salt. The medium was replaced with 100 μL of methanol to dissolve the formazan crystals and the plates were incubated for a further 15 min at room temperature before the absorbance was measured at $\lambda = 570$ nm using a Micro Plate Reader (BioTek Synergy HTX, USA).

Histology/Immunohistochemistry.

Mice were sacrificed by CO_2 asphyxiation at defined time points. Collected tumor tissue was fixed in 10% buffered formalin overnight followed by an additional 24 hours in 70% ethanol. Formalin Fixed Embedded Tissue was cut using microtome with 10 um thickness. Tissue slides were dried overnight and subjected to de-paraffinization in xylene. For antigen retrieval, slides were boiled for 10 minutes in 10 mM sodium citrate pH 6 solution for all antibodies. ImmPRESS detection system (Vector Laboratories) was used for detection of TFE3 (TFE3 (P-16): sc-5958, Santa Cruz, USA). Staining was visualized using 3,3′-Diaminobenzidine (DAB) (Sigma, Saint Louis, MO, FAST 3,3′-Diamino benzidine) and slides were counterstained with hematoxylin.

Immunofluorescence microscopy.

Cells grown on glass coverslips with and without drug treatment were washed with PBS and fixed with 4% paraformaldehyde on ice for 15 min. After fixation, cells were washed with

PBS and then permeabilized with 0.1% Triton X-100 in PBS at room temperature for 20 min followed by blocking with 2.5% Bovine Serum Albumin (BSA) in PBS for 90 minutes. Cells were then incubated with the indicated primary antibodies; rabbit anti phospho-ribosomal S6 Ser235/236 (Cell signaling technology, #2211, at 10ug/mL), rabbit anti phospho-4EBP-1 (Cell signaling technology #2855 and #9451, at 20ug/mL), rabbit anti phosphor-AKT (ser473) (Cell signaling technology #4060 at 10ug/mL), Mouse anti IRS-2 (Millipore #MAB S15 at 10 ug/mL), rabbit anti LDH (Santa Cruz Biotechnology #sc-33781 at 10ug/mL), rabbit anti TFEB (Bethyl Laboratory #A303–673A at 10 ug/mL), rabbit anti TFEC (Sigma #AV32279), rabbit anti N-terminal TFE3 (Santa Cruz Biotechnology #sc-33781) and IR in IF buffer (PBS containing 2.5% BSA and 0.1% triton X-100) overnight at 4^{o} Celsius temperature. Cells were washed three times with PBS and incubated with the corresponding secondary antibodies conjugated to Alexa Fluor 633-conjugated goat anti-mouse IgG or Alexa Fluor 633-conjugated goat anti-rabbit IgG (1:2,000; Life Technologies) in IF buffer for 30 min at room temperature. PBS washed coverslips were mounted onto glass slides with Vectashield antifade mounting medium (Vectorlabs, USA). Images were acquired on EVOS-FLc AMEFC4300 fluorescence imaging system (Thermoscientific, USA) with the same acquisition parameters for each group. Images taken were processed and quantified with ImageJ software (NIH).

SiRNA mediated TFE3 silencing.

Cells were transfected with siRNAs targeting TFE3, (Silencer® Select siRNAs, Sigma #s14032, USA) or a scrambled siRNA (*Silencer*™ Select Negative Control No. 1 siRNA, Sigma #4390843, USA). RP-R07 cells were cultured in 6-well plates until 50%−60% confluence, transfected with TFE3-siRNA or scramble with a final concentration 100 nM using Lipofectamine™ RNAiMAX Transfection Reagent (Invitrogen #13778075, USA) according to the manufacturer's instructions. At 72 h after transfection, cells were harvested for qRT-PCR or Immunofluorescence analyses.

In vivo animal treatments.

The Institute Animal Care and Use Committee at Indiana University approved all mouse protocols used in this study. Mice were housed in a BSL-2 level animal facility maintained on a 12-h light/dark cycle, at a constant temperature (22±2°C) and relative humidity (55±15%). NSG mice for *in-vivo* study were purchased from an in-house colony maintained at Indiana University. Approximately six-week old NSG mice were implanted subcutaneously with ~ 3 mm^3 pieces of RP-R07 tumor and allowed to grow until tumors reached 200 mm^3 in volume prior to treatment with either vehicle, Rapamycin (EMD chemicals, USA), MLN0128 (kindly provided by Millenium Pharmaceuticals, USA) or BEZ-235 (kindly provided by Novartis Pharmaceuticals, USA). Tumor bearing mice received therapy with Rapamycin (2 mg/kg daily; i.p. injection). MLN0128, (3 mg/kg, three times a week; i.p. injection), BEZ-235 (25 mg/kg daily-five days per week; oral gavage) or vehicle (daily-five days per week; oral gavage). Throughout the study all mice receiving therapy were weighed twice weekly to monitor for toxicities. Tumor growth was assessed by serial caliper measurements twice weekly.

Statistical Analysis

Statistical analysis was performed GraphPad (San Diego, CA, USA) prism software. Differences among experimental groups were tested by Student's t test or for variances by ANOVA followed by Tukey post-test. P-values less than 0.05 were considered to be statistically significant.

RESULTS

Establishment of RP-R-07t patient-derived xenograft (PDX) model.

A 24-year-old Caucasian male patient with no previous medical history presented with a symptomatic, large tumor mass in the right kidney. The patient underwent nephrectomy which revealed a high grade, mixed clear cell/papillary RCC. Further analysis driven by his young age led to the diagnosis of MiT family tRCC associated with an Xp11.2 translocation/ *TFE3* gene fusion by FISH analysis. The patient developed rapidly growing metastases, initially in the lymph nodes and lungs. Therapies with a vascular endothelial growth factor receptor tyrosine kinase inhibitor (sunitinib), a mTOR inhibitor (everolimus), and chemotherapeutic drugs (doxorubicin and gemcitabine), had no effect on tumor progression and eventually the patient deceased within one year from diagnosis.

During the course of the disease, we obtained a lymph node biopsy (Fig. 1A). The resected tissue was partitioned into ~3–5 mm^3 pieces, processed, and implanted subcutaneously into six-week-old female NOD-SCID gamma (NSG) mice. We allowed tumors to grow to a size of ~1,500 mm^3 during the engraftment phase, at which point they were harvested for the following purposes: 1) establishment of a cell line, 2) further expansion through serial passaging in NSG mice (Fig. 1B), and 3) histological and molecular characterization. To develop the RP-R07 cell line, we adopted a conditional reprogramming method utilizing Rho-associated, coiled-coil containing protein kinase (ROCK) inhibitor and irradiated NIH-3T3 murine fibroblasts . We evaluated whether our PDX pre-clinical model maintained histological features of the original lymph node metastasis. The cellular architecture in our PDX tumor model remained remarkably faithful to the tumor original morphology (Fig. 1C), exhibiting similar mixed papillary and clear cells characteristics. Furthermore, our PDX model demonstrated the same strong TFE3 nuclear immunoreactivity observed in the original biopsy.

Identification of SFPQ-TFE3 fusion in RP-R07 by RNA-seq.

To identify the specific *TFE3* fusion gene and chromosomal breakpoint in our pre-clinical model, we sequenced RNA isolated from RP-R07 cells. Reverse transcription using multiple oligonucleotides complementary to *TFE3* was followed by next generation sequencing to characterize *TFE3* fusion transcripts. A fusion transcript was identified spanning the *SFPQ* gene on chromosome 1p and the *TFE3* gene on chromosome Xp. The genomic coordinates of the RNA fusion junction localized to specific chromosomal break-points (Chr1:35652601; ChrX:48895638) (Fig. 1D). This location corresponds to the end of *SFPQ* exon 9 and the beginning of *TFE3* exon 5. The expression of the *SFPQ-TFE3* fusion transcript was confirmed by subjecting cDNA from RP-R07 to RT-PCR amplification with 5'-*SFPQ* and 3'-*TFE3* primers and, as a control, primer sets for the *NONO-TFE3* (25) and

PRCC-TFE3 fusions (26). Only the *SFPQ-TFE3* hybrid transcript with a predicted size of 375bp was observed in RP-R07 (Fig. 1E), while the *NONO-TFE3* and *PRCC-TFE3* fusions were not detected. Using the same *SFPQ-TFE3* primers, we did not detect the presence of the *SFPQ-TFE3* transcript in the *NONO-TFE3* fusion-bearing UOK-109 cell line (25) (Fig. 1F), the *PRCC-TFE3* fusion-bearing UOK-146 cell line (26), the UMR-C2 ccRCC cell line, or the HK-2 human renal cell tubule cell line.

TFE3 nuclear expression is characteristic of tRCC.

Xp11.2 tRCC contains fusion genes that encode chimeric proteins consisting of the N-terminal portion of different translocation or inversion partners fused to the C-terminal portion of TFE3 (3). Therefore, chromosomal rearrangements involving the *TFE3* gene at Xp11.2 are characterized by strong nuclear immunoreactivity for the C-terminal portion of TFE3 regardless of *TFE3* fusion gene partner (27). We identified enhanced nuclear immunoreactivity of C-terminal TFE3 in three different tRCC models: RP-R07 (*SFPQ-TFE3*), UOK-109 (*NONO-TFE3*), and UOK-146 (*PRCC-TFE3*). In contrast, nuclear immunoreactivity was low in the ccRCC cell line, UMR-C2 (Fig. 1G). However, despite the common presence of C-terminal TFE3 immunoreactivity, each tRCC model demonstrated distinct expression levels and distribution patterns. Co-localization analysis (Fig. 1H) represents the level of C-terminal TFE3 nuclear localization. The UOK-109 model showed the highest C-terminal TFE3 nuclear immunoreactivity with a dense expression pattern ($R=0.78$, UOK-109-UMR-C2 $P<0.0001$). RP-R07 demonstrated moderate C-terminal TFE3 nuclear immunoreactivity with a diffuse expression profile ($R=0.69$, RP-R07-UMR-C2 $P<0.0001$). Whereas, the UOK-146 model demonstrated the lowest C-terminal TFE3 nuclear immunoreactivity with a mixed expression pattern involving diffuse and speckle components ($R=0.62$, UOK-146-UMR-C2 $P<0.0001$).

ChIP-seq based TFE3-DNA binding profiling reveals TFE3 occupancy of genomic regions with consensus E-box motifs both in vitro and in vivo.

We performed ChIP-seq to explore the DNA binding landscape of TFE3 in RP-R07 (patient derived cells) and RP-R07t (patient derived xenograft) and UOK-146 cells. The Western blot result demonstrates the specificity of the antibody recognizing TFE3 in all three cells RP-R07, UOK-146 and UOK-109 (Supplementary Fig. S1). ChIP-seq in RP-R07 cells identified 3032 significant TFE3 peaks. ChIP-seq from RP-R07t identified 856 significant TFE3 peaks (Supplementary Table S1, Table S2). A comparison of TFE3 ChIP-seq signal across all bound regions revealed a strong overlap between RP-R07 and RP-R07t (Fig. 2A), indicating that the *in vitro* and *in vivo* model have similar TFE3 binding profiles. Furthermore, we have also observed identical binding profile of TFE3 in UOK-146 cells (Supplementary Fig. S2). An unbiased search for over-represented sequence motifs in TFE3-bound regions by MEME-ChIP identified the known TFE3 target E-box motif (CACGTGA) as the most enriched motif in both cell line and tumor samples (Fig. 2B). Notably, AP-1 (TGACTCA) and ETS (AGGAA) binding motifs are the second and third most enriched motifs in TFE3 bound regions in the cell line. The identified TFE3 peaks distribution in RP-R07 and RP-R07t are presented in Supplementary Fig. S3 and Fig. S4, respectively.

TFE3 target genes are associated with the PI3K/AKT/mTOR signaling pathway.

We applied our ChIP-seq results to study the molecular pathways targeted by the *SFPQ-TFE3* fusion gene product using pathway analysis bioinformatics tools, including KEGG, PANTHER, and WIKI. Comprehensive panels of 287 KEGG pathways, 96 PANTHER pathways, and 403 WIKI tools pathways associated with the *SFPQ-TFE3* fusion gene product are listed in Supplementary Table S3, Supplementary Table S4, and Supplementary Table S5, respectively. Based on these results, we noted that the PI3K/AKT/mTOR axis was consistently ranked as a top significantly influenced pathway in all three analysis methods (Fig. 2C-E). When looking closely at our ChIP-seq results, we were able to identify of SFPQ-TFE3 targeted genes related to the PI3K/AKT/mTOR pathway, such as *PI3KCA, TSC1, AKT3, PTEN, 14–3-3, ITGB1, IGFR1*, and *IRS-1* (Fig. 2F).

MicroRNAome landscape profiling reveals molecular pathway signatures of RP-R-07.

After profiling the TFE3 transcriptional architecture in our tRCC model, we further studied its post-transcriptional microRNAome landscape. Expression profile analysis of the whole microRNAome in tRCC (RP-R07t), ccRCC and pRCC PDX models (also established in our lab) was performed using TaqMan® low-density array human microRNA card set A+B. These are pre-loaded arrays with TaqMan Gene Expression Assays for mature miRNAs. Despite overlapped histological features of ccRCC and pRCC PDX in our tRCC PDX (Fig. 3A), several miRNAs showed variable expression among the three varied subtypes (Fig. 3B). Unsupervised hierarchical clustering employing one minus Pearson correlation with average linkage further classified tRCC, ccRCC, and pRCC into three well-defined clusters and differentially expressed miRNA into nine well-defined clusters (Fig. 3C). Cluster 3 had the greatest deviation of miRNA expression, with a > 2-fold change of expression in our tRCC model as compared to ccRCC and pRCC PDX models (Fig. 3D). To further understand the biological impact of differentially expressed miRNA in our tRCC model, we used DIANA-miRPath to perform a pathway analysis of the miRNA in cluster 3. Hierarchical clustering heatmap revealed significantly targeted pathways by the miRNA signature in cluster 3 (Fig. 3E). The top significantly enriched pathways based on the number of miRNA targeted genes associated with each pathway (Fig. 3F) were “Pathways in cancer” (P=1.11E-16), “PI3K-Akt signaling pathway” (P=4.91E-09), “Proteoglycans in cancer” (1.11E-16), “Focal adhesion” (P=6.26E-10), “Viral carcinogenesis” (P=1.11E-16), “MAPK signaling pathway” (P=0.000121), and “Hippo signaling pathway” (P=1.11E-16). A complete list of the statistically enriched pathways targeted by differential expression of miRNA in cluster 3 is available in Supplementary Table S6. Enriched KEGG PI3K/AKT signaling pathway visualization (Supplementary Fig. S5) shows that almost all predicted genes in this pathway are targeted by aberrantly expressed miRNA in cluster 3, including *PI3KCA, AKT1, IRS1, RPS6, TSC1, eIF4BP1*, and mTOR among others. A complete list of targeted genes in the PI3K/AKT signaling pathway with their associated miRNA from cluster 3 is reported in Supplementary Table S7.

Upregulation of PI3K/AKT/mTOR pathway in tRCC.

The PI3K/AKT (28) and mTOR (29) signaling pathways function interdependently to regulate cellular growth, proliferation, angiogenesis, and survival. Their roles are so

intertwined such that they are often unified into one unique signaling axis, PI3K/AKT/mTOR. Oncogenic dysregulation of this pathway has been implicated in a variety of tumors, including ccRCC (30). Thus, we were interested in testing whether this pathway is also involved in tRCC, starting with the examination of P13K/AKT/mTOR activity in our tRCC panel. Phosphorylation of S6 ribosomal protein (S6rp) and 4E-BP1 occurs at the end of the P13K/AKT/mTOR signaling cascade to facilitate translation. Thus, by measuring the immunoreactivity of phosphorylated S6rp (31) and 4E-BP1, we can gauge the level of P13K/AKT/mTOR activation. Using a quantifiable immunofluorescence technique, our results suggest a higher level of phospho-S6rp (Fig. 4A, C) expression in the tRCC cell lines as compared to the ccRCC cell line. The expression levels of phospho-4E-BP1 in the tRCC cell lines were also higher than those observed in the ccRCC cell line as well (Fig. 4B, D). These results suggest that the PI3K/AKT/mTOR pathway is disproportionately upregulated in tRCC regardless of TFE3 gene fusion partner.

Effective in vitro multi-nodal P13K/AKT/mTOR inhibition in RP-R07.

Based on the dysregulation of the P13K/AKT/mTOR pathway, we tested the anti-tumor effect of inhibiting this pathway in tRCC cell lines, as a potential therapeutic strategy. We designed three vertical inhibition schemas to target the PI3K/AKT/mTOR axis at different points within the pathway: 1) PI3K/AKT axis inhibition with the P13K inhibitor BKM-120, 2) m-TOR axis inhibition with the pan-mTOR inhibitor MLN0128, and 3) simultaneous inhibition of the PI3K/AKT and mTOR axis with the dual P13K/mTOR inhibitor BEZ-235. We **first examined whether the drug response** profiles of our tRCC panel were reflective of the lack of response to anti-neoplastic agents that the patients experienced. RP-R07, UOK 109, and UOK-146 cells were exposed to increasing concentrations of sunitinib, doxorubicin, and gemcitabine for 96 hours (Fig. 4E-G). The tRCC cell lines were relative insensitive to these anti-neoplastic agents except for gemcitabine. Thus, we evaluated our multi-nodal PI3K/AKT/mTOR inhibition strategy *in vitro*. An MTT assay was performed after cells were treated with different concentrations of BKM-120, MLN0128, rapamycin or BEZ-235 for 96 hours to assess the anti-tumor activity of these agents (Fig. 4H-J, Supplementary Fig. 6). BKM-120 treatment inhibited cellular proliferation in a concentration-dependent manner with IC50 values of 420, 373.6 and 714 nM for RP-R07, UOK-109, and UOK-146, respectively (Fig. 4K). The dual TORC1/TORC2 inhibitor MLN0128 demonstrated greater anti-proliferative effect than the PI3K inhibitor BKM-120 with 10-fold lower IC50 values (RP-R07: IC50=49.4 nM, UOK-109: IC50=24.3 nM, and UOK-146: IC50=8.18 nM). Treatment with dual PI3K/mTOR inhibitor BEZ-235 had the lowest IC50s in our tRCC panel (RP-R07: IC50=12.2 nM, UOK-109: IC50=13.41 nM, and UOK-146: IC50= 7.03 nM). Taken together, these results suggest that simultaneous vertical inhibition of the PI3K/AKT/mTOR axis with a dual PI3K/mTOR inhibitor provides a greater anti-proliferative effect *in vitro* as compared to P13K/AKT or mTOR inhibition alone for the treatment of tRCC.

Attenuation of PI3K/AKT/mTOR downstream targets by BEZ-235.

To validate whether the anti-proliferative effect of BEZ-235 in RP-R07 cells was associated with biochemical attenuation of the PI3K/AKT/mTOR pathway, we assessed the phosphorylation and expression levels of selected key nodes by immunofluorescence.

BEZ-235 treatment inhibited phosphorylation of 4EBP-1 at Serine-65 (78% inhibition; P<0.0001) and Threonine-37 (58% inhibition: P<0.0001) (Fig. 5A, B). Corresponding signal reduction of phosphorylated AKT at Serine-473 (27% inhibition; P<0.001) and phosphorylated S6rp at Serine 240/244 (63.3% inhibition; P<0.0001) was also observed. Additionally, we observed decreased expression of PI3K/AKT/mTOR possible downstream target such as lactate dehydrogenase (54.4% inhibition; P<0.0001), IRS-1 (33.9% inhibition; P<0.0001), TFE3 (24.1% inhibition; P<0.0001), TFEB (53% inhibition; P<0.0001) and TFEC (41% inhibition; P<0.0001).

TFE3 silencing attenuates PI3K/AKT/mTOR signaling and suppresses IRS-1 expression and cell proliferation in RP-R07.

We have shown that wild type TFE3 is a potential downstream target of PI3K/AKT/mTOR axis as PI3K/mTOR inhibition suppresses TFE3 expression. Therefore, to further determine whether TFE3 inhibition by PI3K/AKT/mTOR directly affects cellular biological function, we assessed the effect of siRNA mediated TFE3 silencing on RP-R07 cell proliferation. First, we confirmed the efficacy of our siRNA treatment by assessing TFE3 endogenous mRNA transcript level and protein expression after cells treatment with TFE3-siRNA and negative control-siRNA, scramble RNA (Fig. 6A). Further, decrease of protein expression levels of TFE3 following TFE3-siRNA treatment was observed by immunofluorescence (Fig. 6B, C). Next, we assessed whether inhibition of TFE3 provides regulatory feedback on PI3K/AKT/mTOR signaling axis. Decrease expression of phospho-4EBP1 (Fig. 6D, F) and phospho-S6 ribosomal (Fig. 6E, G) was observed in TFE3-siRNA treated cells compared to scramble RNA treated cells. This result suggests the possible regulatory role TFE3 on PI3K/AKT/mTOR pathway *via* a feedback loop mechanism in which TFE3 is not only downstream target of PI3K/AKT/mTOR pathway, but also directly regulates this signaling pathway. As far as the regulatory mechanism of TFE3 on PI3K/AKT/mTOR pathway, we propose that this may be mediated through TFE3 target genes which are upstream effectors of this signaling axis. Based on our ChIP-seq results (Fig. 2F, Supplementary Table 2), TFE3 binds to IRS-1, an upstream effector of PI3K/AKT/mTOR (32). Therefore, we further validated the transcriptional regulatory role of TFE3 on IRS-1 by assessing the effect of TFE3 inhibition on IRS-1 expression. SiRNA mediated silencing of TFE3 decreased endogenous expression of IRS-1 mRNA transcript compared to scramble RNA treatment (P<0.01) (Fig. 6H). Next, the analysis of immunofluorescence images further demonstrated the decrease of IRS-1 protein expression following TFE3-siRNA treatment compared to scramble RNA treatment (P<0.001) (Fig. 6I, J). Finally, TFE3 silencing inhibited cell proliferation of RP-R07 in a time-dependent fashion (Fig. 6K). Following TFE3-siRNA treatment at 96 hrs and 110 hrs, the cell number was significantly reduced (96 hrs P=0.04, 110 hrs P< 0.00001) in RP-R07 compared to the non-silencing control siRNA transfected cells and non-treated cells.

Effective in vivo multi-nodal P13K/AKT/mTOR inhibition in RP-R07.

Next, we investigated the anti-proliferative effect of MLN0128 and BEZ-235 *in vivo*. We also wanted to assess the efficacy of rapamycin, an mTOR complex-1 (mTORC1) inhibitor, as a comparator since the mTOR inhibitors that are FDA approved in the treatment of RCC, everolimus and temsirolimus, have a similar mechanism of action (33). Everolimus and

temsirolimus have shown limited clinical activity in RCC (34–37), in part due resistance mechanism(s) *via* mTORC2-mediated rebound AKT hyperphosphorylation. Therefore, we postulated that MLN0128 and BEZ-235 could provide superior anti-tumor effects as compared to rapamycin given their ability to impact this resistance pathway. To test these drugs, NSG mice bearing subcutaneously implanted RP-R07 xenografts were treated with MLN0128 (3 mg/kg), rapamycin (2 mg/kg), or BEZ-235 (25 mg/kg) for 28 days. The vehicle and treatment group mice (5 mice per group) maintained their body weight throughout, incurring in modest weight loss (Supplementary Fig. S7). Treatment of RP-R07 xenografts with MLN0128, rapamycin, and BEZ-235 resulted in decreased tumor weight (Fig. 6L) compared to the vehicle control. However, only treatment with BEZ-235 resulted in a statistically significant lower tumor weight when compared to vehicle control ($P<0.01$). RP-R07t cells of the tumor in the BEZ-235 treated group appeared smaller than those in the vehicle (Fig. 6M), indicating inhibition of mTOR pathway (38). The proliferation marker Ki67 was reduced in the BEZ-235 treated group as compared to the untreated control (Fig. 6M, N), indicating inhibition of cell cycle (90% inhibition, $P<0.0001$). The *in vivo* immunostaining replicated the *in vitro* results demonstrating that BEZ-235 significantly reduced the phosphorylation level of S6 ribosomal protein (83% inhibition, $P<0.0001$) (Fig. 6M, O). The analysis of microvessel density, as measured by CD31 staining, revealed significant inhibition of tumor angiogenesis in BEZ-235 treated RP-R07 tumors (56% inhibition at day 28; $P<0.0001$) compared to vehicle (Fig. 6M, P). Overall, these data suggest the therapeutic efficacy of a multi-nodal P13K/AKT/mTOR inhibition strategy for TFE3-tRCC (Supplementary Fig. S8).

DISCUSSION

Therapeutic strategies to effectively treat MiT family translocation renal cell carcinoma have yet to be established. More importantly, there is a clinical need for evidence-based treatments, as a significant number of patients, likely underestimated by histological misclassification, may be afflicted by this subtype of RCC. In our study, we have characterized the DNA binding landscape of a TFE3 gene fusion product by ChIP-seq using our recently established PDX model bearing a SFPQ-TFE3 fusion. TFE3 binding to genomic regions containing E-box motif was confirmed, and 3032 TFE3 binding sites were associated with 2213 putative TFE3 target genes. Interestingly, our ChIP-seq data also indicate TFE3 binding on ETS and AP-1 binding sites. TFE3 binding on ETS binding motif is consistent with previous reports (3), while TFE3 binding on AP-1 binding site has not been previously reported. ETS and AP-1 binding sites are known to be enriched at enhancers of genes that promote epithelial-mesenchymal transition and cellular migration and invasion (24). Pathway analysis using KEGG, PANTHER and Wiki tools identified the PI3K/AKT/mTOR axis as the top significantly influenced pathway. Specific TFE3 target genes were also associated with this pathway, such as *PI3KCA*, *AKT3*, *IRS-1*, *TSC-1*, *EIF4B*, *VEGFR-2,* suggesting that the PI3K/AKT/mTOR axis represents a rational therapeutic target for this disease.

MicroRNAs (miRNA) are small RNA molecules with 19–23 nucleotide length which act as either tumor promoters or tumor suppressors by targeting the transcription and translation of specific genes. The differential miRNA signature in ccRCC compared to normal kidney

tissues has been well established, and specific miRNAs differences have been identified in metastatic ccRCC (39) (20). We used microarray technology to evaluate the miRNA expression profile of our tRCC model, and observed a distinct miRNA expression profile as compared to pRCC and ccRCC models, despite the presence of mixed papillary/clear cell histologic features. Our results are consistent with recent miRNA profiling of Xp11 tumors bearing SFPQ-TFE3 and ASPSCR1-TFE3 (40), demonstrating distinct miRNA profiles against published data set of ccRCC and pRCC (41). Interestingly, despite different tumor panels and slight difference in our clustering algorithm and method, we also found that tRCC miRNA expression profile is closer to ccRCC compared to pRCC (40). Moreover, our bioinformatic tools indicated that the differential expression of miRNAs could be linked to several targets genes and pathways. Consistent with our ChiP-seq data, PI3K/AKT/mTOR was identified once again as a pathway with significant (P=4.91E-9) association with the miRNA signatures in RP-R07. Similar predicted miRNAs target genes associated with the PI3K/AKT/mTOR pathway, as seen in ChIP-seq, were identified as well. It is noteworthy that some pathways associated with differential miRNA expression identified in our study are the same miRNA associated pathways identified in previous work (40) using larger panel of tRCC tumors. These miRNAs associated pathways include PI3K pathway, cell cycle, p53, lysine degradation, erbB signaling, and wnt signaling pathway. However, different pathways identified in our analysis may due to the fact that the tRCC tumor panels involved in previous work consisted of SFPQ-TFE3 and ASPSCR1-TFE3 tumors while we focused on a SFPQ-TFE3 model. Aberrant activation of PI3K/AKT/mTOR pathway itself has been reported in RCC (42). Although previous studies have demonstrated the association of AKT/mTOR pathway (3) and upregulated phosphor-S6 (43) with tRCC, our results further support the role of PI3K/AKT/mTOR pathway in tRCC as a potential target for therapeutic interventions.

Data integration of tRCC molecular signatures is a valuable resource to generate new hypotheses regarding therapeutic targeted pathways. Therefore, we used a panel of tRCC models to test the hypothesis whether inhibition of the PI3K/AKT/mTOR axis would lead to anti-tumor response. First, we verified that the P13K/AKT/mTOR signaling is overexpressed in our tRCC panel by upregulation of phospo-S6rp and phospho-4E-BP1 protein expression. Then, we enacted a variable, multi-nodal P13K/AKT/mTOR inhibition strategy using three treatment arms to examine the effects of blocking this pathway at different points *in vitro* and *in vivo*: 1) PI3K inhibition with BKM-120, 2) pan-mTOR inhibition with MLN0128, and 3) simultaneous vertical inhibition of PI3K and mTOR with BEZ-235. While all three treatment arms had a greater anti-proliferative effect as compared to the MET inhibitor crizotinib, BKM-120 had a modest effect, which is possibly due to inadequate inhibition by targeting PI3K axis alone. In contrast, MLN0128 and BEZ-235 potently inhibited proliferation of all tRCC cells models tested in a concentration-dependent fashion, with BEZ-235 exerting the greatest effect. While the three therapeutic agents had similar treatment trends across our tRCC panel, there were differential IC50 values amongst the tRCC models bearing distinct TFE3 gene fusions. The tRCC models included in our study did not show a significant response to the MET inhibitor crizotinib. These results seem to be in contrast with previous work (44) that suggests an inhibitory effect of MET inhibition in a tRCC model with ASLP-TFE3 fusion. One possible explanation for this difference is that

MET upregulation may be specific for ASPL-TFE3 fusion and our tRCC panels do not have ASPL-TFE3 fusion. These results may also imply differential regulatory pathways in a fusion partner-dependent fashion and support previous report with differential cathepsin-k expression in tRCC(45). Thorough discussion and analysis on the role of MET inhibition strategy in tRCC has been recently reported (3). BEZ-235 was the only treatment that resulted in significant tumor reduction *in vivo* compared to the modest tumor growth inhibition by rapamycin or MLN0128 alone. Even though dual mTOR inhibition with MLN0128 conferred greater efficacy of tumor growth inhibition compared to partial mTOR inhibition, possibly due to attenuation of the mTORC2-AKT reactivation mechanism (46), our results suggest that neither form of mTOR blockade in isolation is sufficient to elicit significant tumor control in TFE3-tRCC. These results corroborate our finding in the clinic where the patient did not benefit from single agent treatment with everolimus, a mTOR inhibitor, suggesting the need of alternative therapeutic strategy such as simultaneous PI3K and mTOR inhibition.

Interestingly, tRCC does not present a high mutational burden, as the clinical aggressiveness might suggest (47). As previously reported in tRCC, RP-R-07 tumor did not carry mutations in canonical genes such as *TP53, VHL*, *PIK3CA*, *RAS*, *PTEN,* as per the clinical report. (48). The absence of subtype-specific chromosomal abnormalities, besides the fusion genes, suggests a potential “driver” role of TFE3 in the oncogenesis and response to therapies of tRCC. By using siRNA mediated TFE3 silencing strategy, we showed that attenuated wild type TFE3 expression exerts inhibitory effect on RP-R07 cell proliferation. These data also suggest that dimerization with wild type TFE3 is probably required for the biological effects of chimeric TFE3. Next, we also showed possible feedback regulatory mechanism of TFE3 on PI3K/AKT/mTOR by demonstrating inhibition of PI3K/AKT/mTOR downstream effectors following TFE3-siRNA treatment. To further investigate TFE3 feedback loop regulatory mechanism on PI3K/AKT/mTOR, we examined TFE3 target genes based on our ChIP-seq results. One of TFE3 target genes was IRS-1, an upstream modulator of PI3K/AKT/mTOR axis (3). Using the same TFE3 silencing strategy, we confirmed our ChIP-seq result that TFE3 transcriptionally regulates IRS-1. Furthermore, we showed that TFE3 silencing inhibits IRS-1 expression. IRS-1 is one of upstream effectors of PI3K/AKT/mTOR pathway which is negatively controlled by p70S6 kinase (49). However, our study suggests an alternative positive regulation of IRS-1 by TFE3 that likely bypasses P70S6K regulation, and ultimately results in PI3K/AKT/mTOR aberrant activation. Collectively, our results suggest that targeting PI3K/AKT/mTOR results in TFE3 inhibition, and, ultimately, attenuates its feedback loop activation by downregulating its transcriptional target, IRS-1, one of upstream modulators of the pathway. Although, there is possibility that TFE3 feedback loop mechanism on PI3K/AKT/mTOR may be achieved through other upstream nodes of this signaling axis.

In summary, TFE3 tRCC remains a therapeutic challenge (3). Despite the common mixed clear cell and papillary cell morphology, the reported clinical response to targeted therapies, including VEGF receptor tyrosine kinase and mTOR inhibitors, is modest (50). The results from the use of immune checkpoint inhibitors are still not available. Overall, our results suggest the therapeutic potential of PI3K/AKT/mTOR inhibition in tRCC patients. We identified that simultaneous vertical inhibition targeting PI3K and mTOR had greater anti-

tumor response than single node PI3K or mTOR inhibition. However, due to reported toxicity of BEZ-235 (51), further investigation of the safety and therapeutic potential of PI3K/AKT/mTOR inhibition in tRCC patients as well as efforts to develop new PI3K/AKT/mTOR inhibitors with lower toxicities are need.

Supplementary Material

Refer to Web version on PubMed Central for supplementary material.

Acknowledgments

This study was in part supported by the National Cancer Institute P30 CA016056 (RP) and a research donation from Richard and Deidre Turner and family. We would also like to thank the MTMR and Pathology Core Facilities at Roswell Park Cancer Institute.

Glossary

The abbreviations used are:

tRCC	translocation renal cell carcinoma
ccRCC	clear cell renal cell carcinoma
pRCC	papillary renal cell carcinoma
PDX	patient-derived xenograft
PIK3CA	phosphatidylinositol-4,5-bisphosphate 3-kinase catalytic subunit alpha
ChIP-Seq	chromatin immune precipitation sequencing
miRNA	microRNA
MiT	Micropthalmia transcription factor
NGS	next generation sequencing
RT-qPCR	quantitative reverse transcription polymerase chain reaction
IRS-1	insulin receptor substrate 1
NSG	NOD-SCID gamma

REFERENCES

1. Argani P MiT family translocation renal cell carcinoma. Seminars in diagnostic pathology. 2015;32(2):103–13. [PubMed: 25758327]
2. Argani P, Lae M, Hutchinson B, Reuter VE, Collins MH, Perentesis J, et al. Renal carcinomas with the t(6;11)(p21;q12): clinicopathologic features and demonstration of the specific alpha-TFEB gene fusion by immunohistochemistry, RT-PCR, and DNA PCR. The American journal of surgical pathology. 2005;29(2):230–40. [PubMed: 15644781]

3. Kauffman EC, Ricketts CJ, Rais-Bahrami S, Yang Y, Merino MJ, Bottaro DP, et al. Molecular genetics and cellular features of TFE3 and TFEB fusion kidney cancers. Nature reviews Urology. 2014;11(8):465–75. [PubMed: 25048860]

4. Komai Y, Fujiwara M, Fujii Y, Mukai H, Yonese J, Kawakami S, et al. Adult Xp11 translocation renal cell carcinoma diagnosed by cytogenetics and immunohistochemistry. Clinical cancer research : an official journal of the American Association for Cancer Research. 2009;15(4):1170–6. [PubMed: 19228722]

5. Zhong M, De Angelo P, Osborne L, Keane-Tarchichi M, Goldfischer M, Edelmann L, et al. Dual-color, break-apart FISH assay on paraffin-embedded tissues as an adjunct to diagnosis of Xp11 translocation renal cell carcinoma and alveolar soft part sarcoma. The American journal of surgical pathology. 2010;34(6):757–66. [PubMed: 20421778]

6. Kakoki K, Miyata Y, Mochizuki Y, Iwata T, Obatake M, Abe K, et al. Long-term Treatment With Sequential Molecular Targeted Therapy for Xp11.2 Translocation Renal Cell Carcinoma: A Case Report and Review of the Literature. Clinical genitourinary cancer. 2017;15(3):e503–e6. [PubMed: 28190703]

7. Weterman MA, Wilbrink M, Geurts van Kessel A. Fusion of the transcription factor TFE3 gene to a novel gene, PRCC, in t(X;1)(p11;q21)-positive papillary renal cell carcinomas. Proceedings of the National Academy of Sciences of the United States of America. 1996;93(26):15294–8. [PubMed: 8986805]

8. Argani P, Antonescu CR, Illei PB, Lui MY, Timmons CF, Newbury R, et al. Primary renal neoplasms with the ASPL-TFE3 gene fusion of alveolar soft part sarcoma: a distinctive tumor entity previously included among renal cell carcinomas of children and adolescents. The American journal of pathology. 2001;159(1):179–92. [PubMed: 11438465]

9. Argani P, Lui MY, Couturier J, Bouvier R, Fournet JC, Ladanyi M. A novel CLTC-TFE3 gene fusion in pediatric renal adenocarcinoma with t(X;17)(p11.2;q23). Oncogene. 2003;22(34):5374–8. [PubMed: 12917640]

10. Argani P, Zhong M, Reuter VE, Fallon JT, Epstein JI, Netto GJ, et al. TFE3-Fusion Variant Analysis Defines Specific Clinicopathologic Associations Among Xp11 Translocation Cancers. The American journal of surgical pathology. 2016;40(6):723–37. [PubMed: 26975036]

11. Argani P, Zhang L, Reuter VE, Tickoo SK, Antonescu CR. RBM10-TFE3 Renal Cell Carcinoma: A Potential Diagnostic Pitfall Due to Cryptic Intrachromosomal Xp11.2 Inversion Resulting in False-negative TFE3 FISH. Am J Surg Pathol. 2017;41(5):655–62. [PubMed: 28296677]

12. Argani P, Antonescu CR, Couturier J, Fournet JC, Sciot R, Debiec-Rychter M, et al. PRCC-TFE3 renal carcinomas: morphologic, immunohistochemical, ultrastructural, and molecular analysis of an entity associated with the t(X;1)(p11.2;q21). The American journal of surgical pathology. 2002;26(12):1553–66. [PubMed: 12459622]

13. Goodwin Matthew L, Jin H, Straessler K, Smith-Fry K, Zhu J F, Monument Michael J, et al. Modeling Alveolar Soft Part Sarcomagenesis in the Mouse: A Role for Lactate in the Tumor Microenvironment. Cancer Cell. 2014;26(6):851–62. [PubMed: 25453902]

14. Williams SA, Anderson WC, Santaguida MT, Dylla SJ. Patient-derived xenografts, the cancer stem cell paradigm, and cancer pathobiology in the 21st century. Laboratory investigation; a journal of technical methods and pathology. 2013;93(9):970–82. [PubMed: 23917877]

15. Betschinger J, Nichols J, Dietmann S, Corrin PD, Paddison PJ, Smith A. Exit from pluripotency is gated by intracellular redistribution of the bHLH transcription factor Tfe3. Cell. 2013;153(2):335–47. [PubMed: 23582324]

16. Martina JA, Diab HI, Brady OA, Puertollano R. TFEB and TFE3 are novel components of the integrated stress response. The EMBO journal. 2016;35(5):479–95. [PubMed: 26813791]

17. Strub T, Giuliano S, Ye T, Bonet C, Keime C, Kobi D, et al. Essential role of microphthalmia transcription factor for DNA replication, mitosis and genomic stability in melanoma. Oncogene. 2011;30(20):2319–32. [PubMed: 21258399]

18. Jackson RJ, Standart N. How Do MicroRNAs Regulate Gene Expression? Science's STKE. 2007;2007(367):re1.

19. Butz H, Szabo PM, Khella HW, Nofech-Mozes R, Patocs A, Yousef GM. miRNA-target network reveals miR-124as a key miRNA contributing to clear cell renal cell carcinoma aggressive

behaviour by targeting CAV1 and FLOT1. Oncotarget. 2015;6(14):12543–57. [PubMed: 26002553]

20. Khella HW, Bakhet M, Allo G, Jewett MA, Girgis AH, Latif A, et al. miR-192, miR-194 and miR-215: a convergent microRNA network suppressing tumor progression in renal cell carcinoma. Carcinogenesis. 2013;34(10):2231–9. [PubMed: 23715501]
21. Zheng B, Jeong S, Zhu Y, Chen L, Xia Q. miRNA and lncRNA as biomarkers in cholangiocarcinoma(CCA). Oncotarget. 2017.
22. Zhang X, Zhang M, Cheng J, Lv Z, Wang F, Cai Z. MiR-411 functions as a tumor suppressor in renal cell cancer. The International journal of biological markers. 2017:0. [PubMed: 29192715]
23. Hollenhorst PC, Shah AA, Hopkins C, Graves BJ. Genome-wide analyses reveal properties of redundant and specific promoter occupancy within the ETS gene family. Genes & development. 2007;21(15):1882–94. [PubMed: 17652178]
24. Plotnik JP, Budka JA, Ferris MW, Hollenhorst PC. ETS1 is a genome-wide effector of RAS/ERK signaling in epithelial cells. Nucleic acids research. 2014;42(19):11928–40. [PubMed: 25294825]
25. Clark J, Lu YJ, Sidhar SK, Parker C, Gill S, Smedley D, et al. Fusion of splicing factor genes PSF and NonO (p54nrb) to the TFE3 gene in papillary renal cell carcinoma. Oncogene. 1997;15(18): 2233–9. [PubMed: 9393982]
26. Sidhar SK, Clark J, Gill S, Hamoudi R, Crew AJ, Gwilliam R, et al. The t(X;1)(p11.2;q21.2) translocation in papillary renal cell carcinoma fuses a novel gene PRCC to the TFE3 transcription factor gene. Human molecular genetics. 1996;5(9):1333–8. [PubMed: 8872474]
27. Argani P, Lal P, Hutchinson B, Lui MY, Reuter VE, Ladanyi M. Aberrant nuclear immunoreactivity for TFE3 in neoplasms with TFE3 gene fusions: a sensitive and specific immunohistochemical assay. The American journal of surgical pathology. 2003;27(6):750–61. [PubMed: 12766578]
28. Fresno Vara JA, Casado E, de Castro J, Cejas P, Belda-Iniesta C, Gonzalez-Baron M. PI3K/Akt signalling pathway and cancer. Cancer treatment reviews. 2004;30(2):193–204. [PubMed: 15023437]
29. Tee AR, Blenis J. mTOR, translational control and human disease. Seminars in Cell & Developmental Biology. 2005;16(1):29–37. [PubMed: 15659337]
30. Lin F, Zhang PL, Yang XJ, Prichard JW, Lun M, Brown RE. Morphoproteomic and molecular concomitants of an overexpressed and activated mTOR pathway in renal cell carcinomas. Annals of clinical and laboratory science. 2006;36(3):283–93. [PubMed: 16951269]
31. Pantuck AJ, Seligson DB, Klatte T, Yu H, Leppert JT, Moore L, et al. Prognostic relevance of the mTOR pathway in renal cell carcinoma: implications for molecular patient selection for targeted therapy. Cancer. 2007;109(11):2257–67. [PubMed: 17440983]
32. Shaw LM. The insulin receptor substrate (IRS) proteins: At the intersection of metabolism and cancer. Cell Cycle. 2011;10(11):1750–6. [PubMed: 21597332]
33. Battelli C, Cho DC. mTOR inhibitors in renal cell carcinoma. Therapy (London, England : 2004). 2011;8(4):359–67.
34. Motzer RJ, Escudier B, Oudard S, Hutson TE, Porta C, Bracarda S, et al. Phase 3 trial of everolimus for metastatic renal cell carcinoma : final results and analysis of prognostic factors. Cancer. 2010;116(18):4256–65. [PubMed: 20549832]
35. Motzer RJ, Barrios CH, Kim TM, Falcon S, Cosgriff T, Harker WG, et al. Phase II randomized trial comparing sequential first-line everolimus and second-line sunitinib versus first-line sunitinib and second-line everolimus in patients with metastatic renal cell carcinoma. Journal of clinical oncology : official journal of the American Society of Clinical Oncology. 2014;32(25):2765–72. [PubMed: 25049330]
36. Motzer RJ, Escudier B, McDermott DF, George S, Hammers HJ, Srinivas S, et al. Nivolumab versus Everolimus in Advanced Renal-Cell Carcinoma. The New England journal of medicine. 2015;373(19):1803–13. [PubMed: 26406148]
37. Choueiri TK, Escudier B, Powles T, Mainwaring PN, Rini BI, Donskov F, et al. Cabozantinib versus Everolimus in Advanced Renal-Cell Carcinoma. The New England journal of medicine. 2015;373(19):1814–23. [PubMed: 26406150]

38. Huang S, Bjornsti MA, Houghton PJ. Rapamycins: mechanism of action and cellular resistance. Cancer biology & therapy. 2003;2(3):222–32. [PubMed: 12878853]

39. Butz H, Nofech-Mozes R, Ding Q, Khella HWZ, Szabo PM, Jewett M, et al. Exosomal MicroRNAs Are Diagnostic Biomarkers and Can Mediate Cell-Cell Communication in Renal Cell Carcinoma. European urology focus. 2016;2(2):210–8. [PubMed: 28723537]

40. Marchionni L, Hayashi M, Guida E, Ooki A, Munari E, Jabboure FJ, et al. MicroRNA expression profiling of Xp11 renal cell carcinoma. Human pathology. 2017;67:18–29. [PubMed: 28411178]

41. Munari E, Marchionni L, Chitre A, Hayashi M, Martignoni G, Brunelli M, et al. Clear cell papillary renal cell carcinoma: micro-RNA expression profiling and comparison with clear cell renal cell carcinoma and papillary renal cell carcinoma. Human pathology. 2014;45(6):1130–8. [PubMed: 24703100]

42. Guo H, German P, Bai S, Barnes S, Guo W, Qi X, et al. The PI3K/AKT Pathway and Renal Cell Carcinoma. Journal of Genetics and Genomics. 2015;42(7):343–53. [PubMed: 26233890]

43. Argani P, Hicks J, De Marzo AM, Albadine R, Illei PB, Ladanyi M, et al. Xp11 translocation renal cell carcinoma (RCC): extended immunohistochemical profile emphasizing novel RCC markers. The American journal of surgical pathology. 2010;34(9):1295–303. [PubMed: 20679884]

44. Tsuda M, Davis IJ, Argani P, Shukla N, McGill GG, Nagai M, et al. TFE3 fusions activate MET signaling by transcriptional up-regulation, defining another class of tumors as candidates for therapeutic MET inhibition. Cancer research. 2007;67(3):919–29. [PubMed: 17283122]

45. Martignoni G, Gobbo S, Camparo P, Brunelli M, Munari E, Segala D, et al. Differential expression of cathepsin K in neoplasms harboring TFE3 gene fusions. Modern pathology : an official journal of the United States and Canadian Academy of Pathology, Inc. 2011;24(10):1313–9.

46. Choo AY, Yoon SO, Kim SG, Roux PP, Blenis J. Rapamycin differentially inhibits S6Ks and 4E-BP1 to mediate cell-type-specific repression of mRNA translation. Proceedings of the National Academy of Sciences of the United States of America. 2008;105(45):17414–9. [PubMed: 18955708]

47. Classe M, Malouf GG, Su X, Yao H, Thompson EJ, Doss DJ, et al. Incidence, clinicopathological features and fusion transcript landscape of translocation renal cell carcinomas. Histopathology. 2017;70(7):1089–97. [PubMed: 28106924]

48. Malouf GG, Su X, Yao H, Gao J, Xiong L, He Q, et al. Next-generation sequencing of translocation renal cell carcinoma reveals novel RNA splicing partners and frequent mutations of chromatin-remodeling genes. Clinical cancer research : an official journal of the American Association for Cancer Research. 2014;20(15):4129–40. [PubMed: 24899691]

49. Zhang J, Gao Z, Yin J, Quon MJ, Ye J. S6K directly phosphorylates IRS-1 on Ser-270 to promote insulin resistance in response to TNF-(alpha) signaling through IKK2. The Journal of biological chemistry. 2008;283(51):35375–82. [PubMed: 18952604]

50. Tannir NM, Jonasch E, Albiges L, Altinmakas E, Ng CS, Matin SF, et al. Everolimus Versus Sunitinib Prospective Evaluation in Metastatic Non-Clear Cell Renal Cell Carcinoma (ESPN): A Randomized Multicenter Phase 2 Trial. European urology.2016;69(5):866–74.51. [PubMed: 26626617]

51. Carlo MI, Molina AM, Lakhman Y, Patil S, Woo K, DeLuca J, et al. A Phase Ib Study of BEZ235, Dual Inhibitor of Phosphatidylinositol 3-Kinase (PI3K) and Mammalian Target of Rapamycin (mTOR), in Patients With Advanced Renal Cell Carcinoma. Oncologist. 2016 7;21(7):787–8. [PubMed: 27286790]

TRANSLATIONAL RELEVANCE

Despite the significant progress achieved by targeted therapies in renal cell carcinoma, patients with translocation RCC continue do have a poor outcome. The lack of understating of the biology of this aggressive subtype remains a major hurdle for the development of effective therapies. Thus, we have discovered a key signaling pathway activated by the transcriptional factor TFE3 as the result of the pathognomonic genomic alteration in translocation RCC. Therefore, we have identified an effective combination strategy that can be readily translated to patients with this orphan, deadly disease.

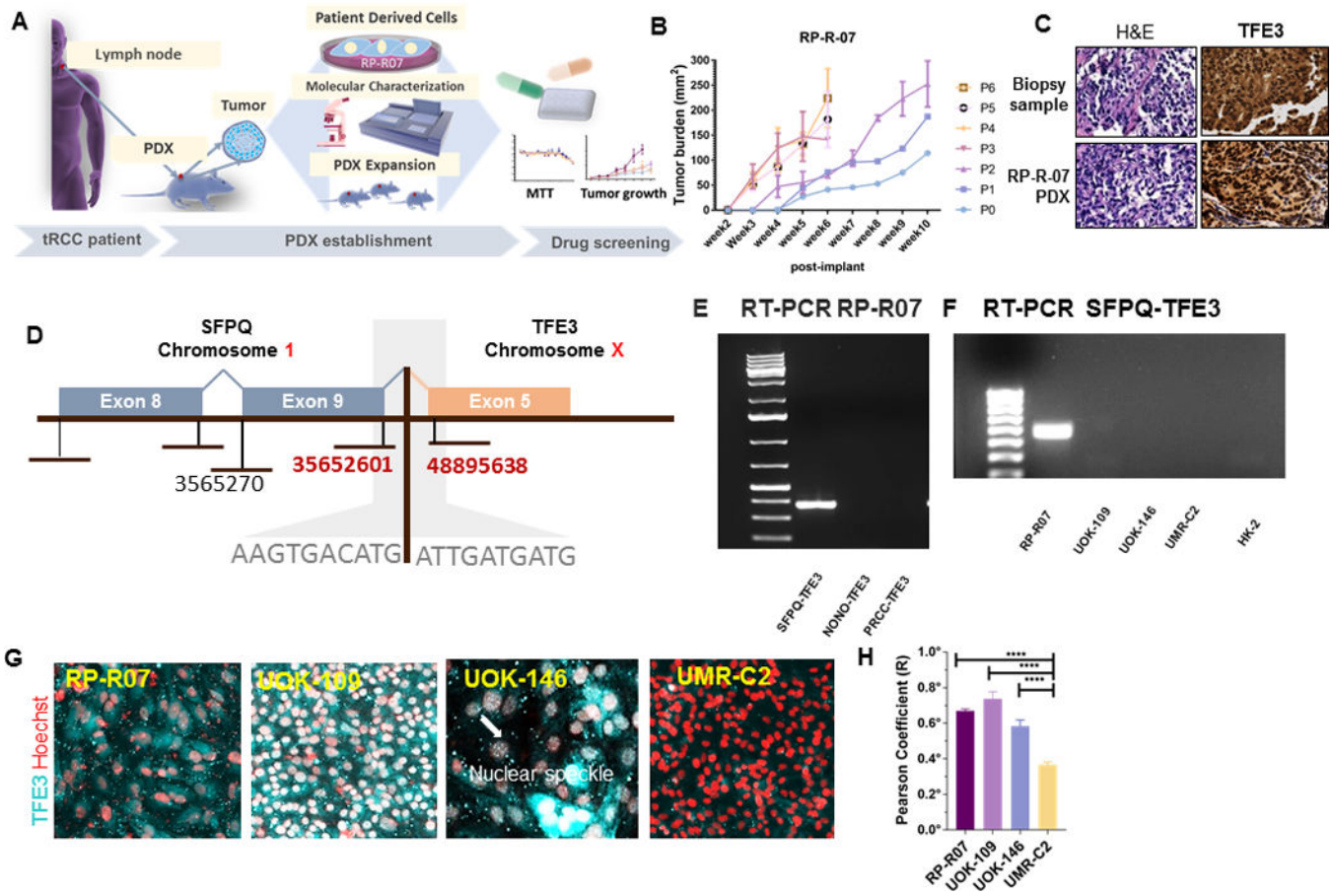

Figure 1. Generation of a patient derived xenograft (PDX) RP-R07t and RP-R07 cells from a tRCC patient.

A. Schematic diagram of development of PDX as a model for therapeutic strategies in the treatment of tRCC patients. B. PDX model demonstrates its ability to self-propagate. B. Growth of primary tumor graft is represented as tumor volume versus time after implantation. Different color indicated different passages. At least four mice were included in each group. C. Faithful resemblance of cellular complexity, architecture and molecular signature of PDX tumor to the patient tumor. Hematoxylin-eosin staining revealed that the PDX model (bottom) recapitulates the histologic appearance of patient tumor, showing characteristic phenotype of mixed papillary architecture and clear or eosinophilic cytoplasm, nested alveolar pattern, voluminous cytoplasm, prominent nucleoli and the presence of psammoma bodies. Molecular signature of X11p translocation, immunoreactivity of nuclear TFE3, is observed in patient biopsy sample (top right) and is preserved in PDX model (bottom right). D. TFE3 fusion architecture by RNA-seq. In-frame fusion transcripts were identified with the chromosomal coordinates corresponding to the fusion position indicated in red (GRCh37/hg19) and the fusion sequence in grey. E. PCR fusion validation in RP-R07 using *SFPQ-TFE3*, *NONO-TFE3*, and *PRCC-TFE3* primers, F. PCR validation in RP-R07, UOK-109, UOK-146, UMR-C2 and HK2 using SFPQ-TFE3 primer. G. Nuclear Immunoreactivity of TFE3 is exclusive for tRCC. Immunofluorescence profile of patient derived cells and cell line stained with the same TFE3 (internal epitope sc-4784) antibody

shows positive nuclear immunoreactivity of TFE3, identified with co-localization (grey white) of nuclear TFE3 (cyan) with DNA stain Hoechst (red) in tRCC cells; RP-R07, UOK-146 and UOK-109 and lower expression ($P<0.005$) of nuclear TFE3 in RCC cell line UMR-C2 H. Co-localization analysis by measuring Pearson correlation coefficient (R) between green channel (TFE3) and red channel (Hoechst) indicating strong nuclear localization of TFE3 in tRCC ($R>0.5$), and significantly lower expression of nuclear TFE3 in UMR-C2. ($R < 0.5$, $P<0.005$). H. Quantitative analysis.

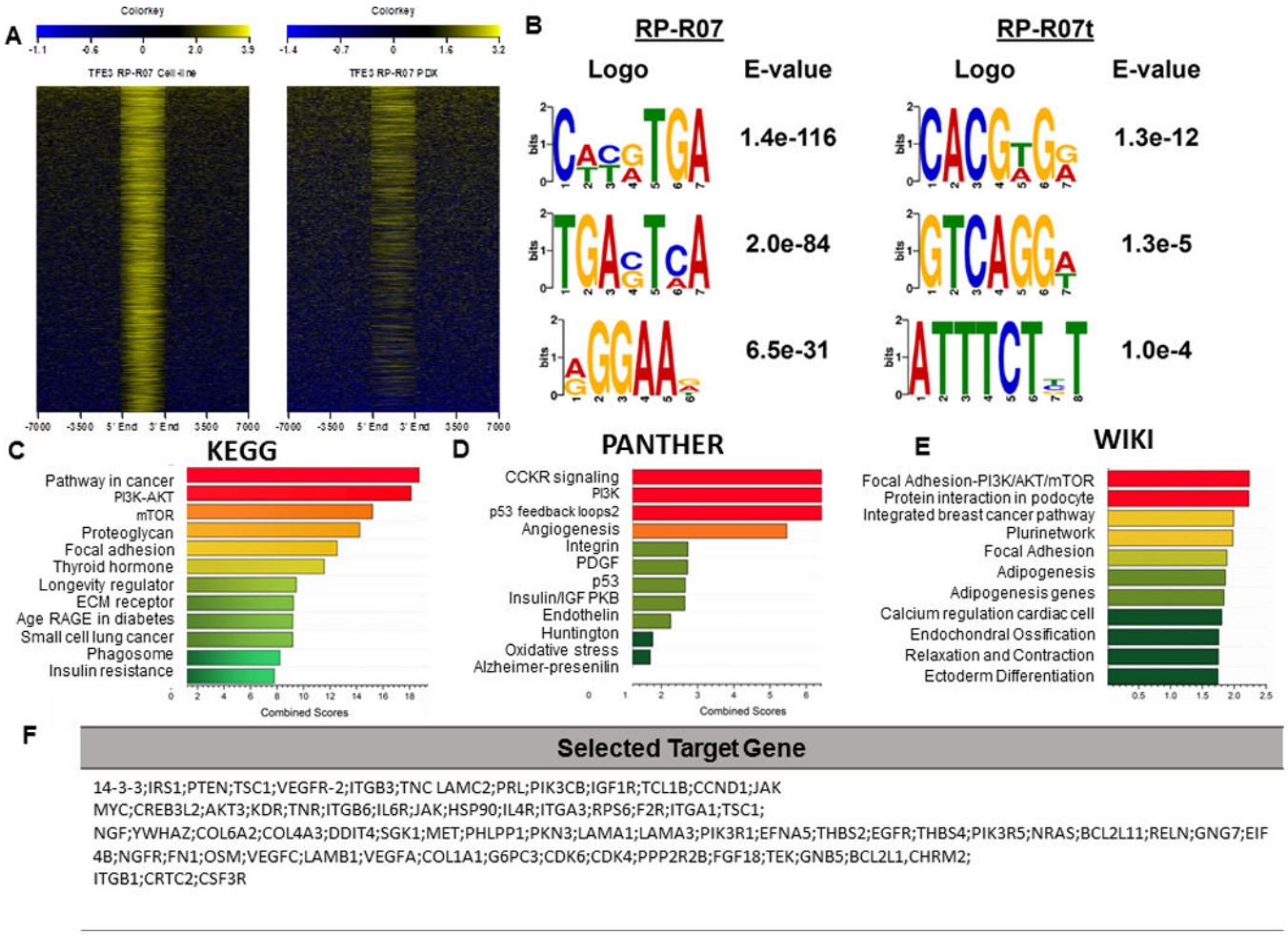

Figure 2. Profiling of TFE3-DNA binding landscape in RP-R07 and RP-R07t by ChIP-seq.

A. Heatmap comparison of TFE33 binding in RP-R07 and RP-R07t at all sites called as bound in either sample. B. The three most enriched sequence motifs identified by the MEME-ChIP program for TFE3 bound regions in RP-R07 or RP-R07t. (C-E). Top 12 pathways associated with TFE3 target genes identified by C. KEGG, D. PANTHER and E. WIKI tools. F. Selected TFE3-targeted genes associated with PI3K/AKT/mTOR pathway.

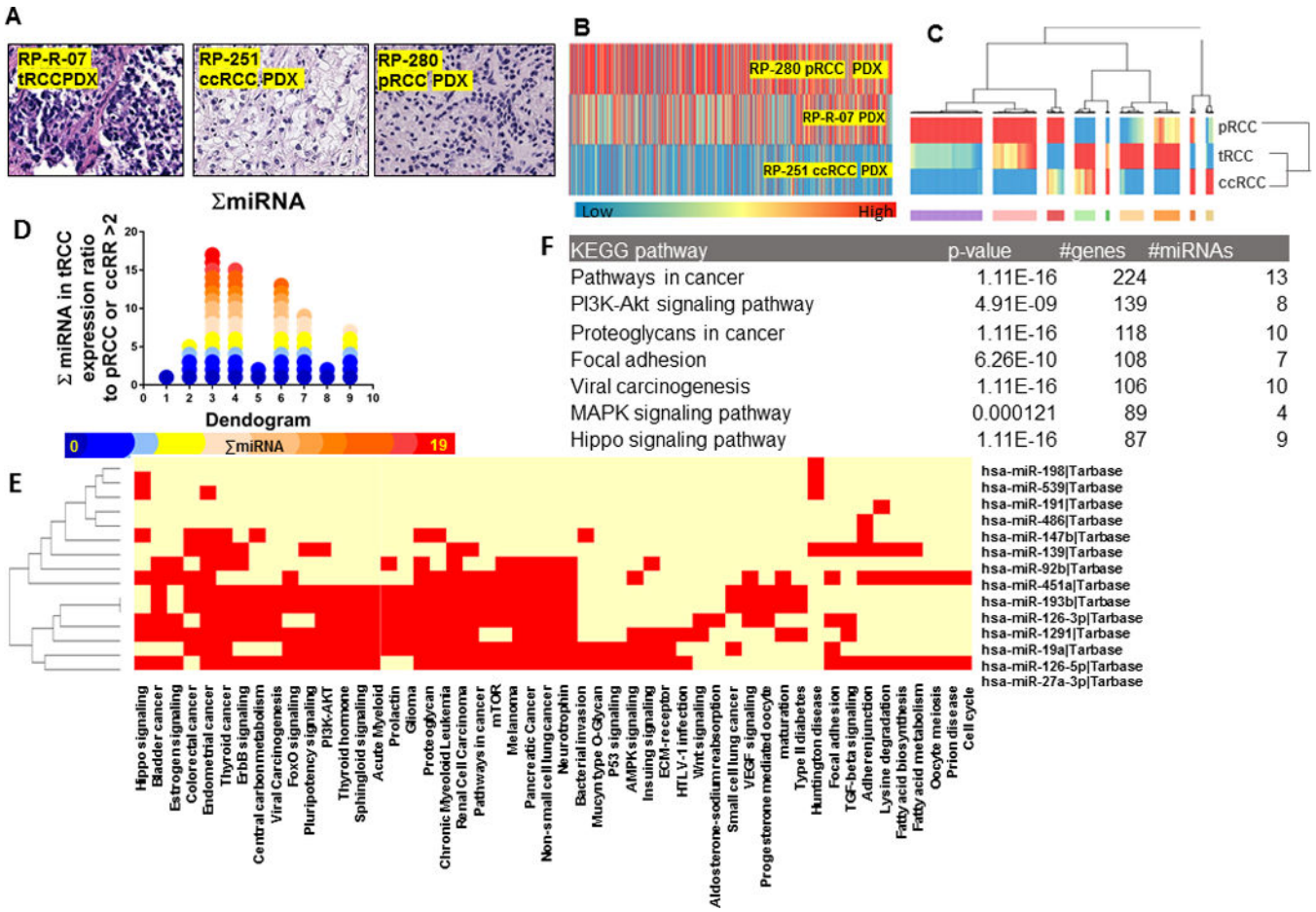

Figure 3. MicroRNA profiling of RP-R07t.

A. IHC staining of RP-R07, pRCC and ccRCC PDX. B. Heatmap showing 786 differential miRNA expression profile. C. Hierarchical clustering of miRNAs expression separate tRCC subtype from pRCC and tRCC D. Number of differentially expressed RP-R07t's miRNA with >2-fold change compared to pRCC and or ccRCC in each cluster in C. E. miRNAs versus pathways heatmap (clustering based on significance levels). F. Top significant KEGG pathway associated with differentially expressed miRNA based on the number of associated miRNA target genes.

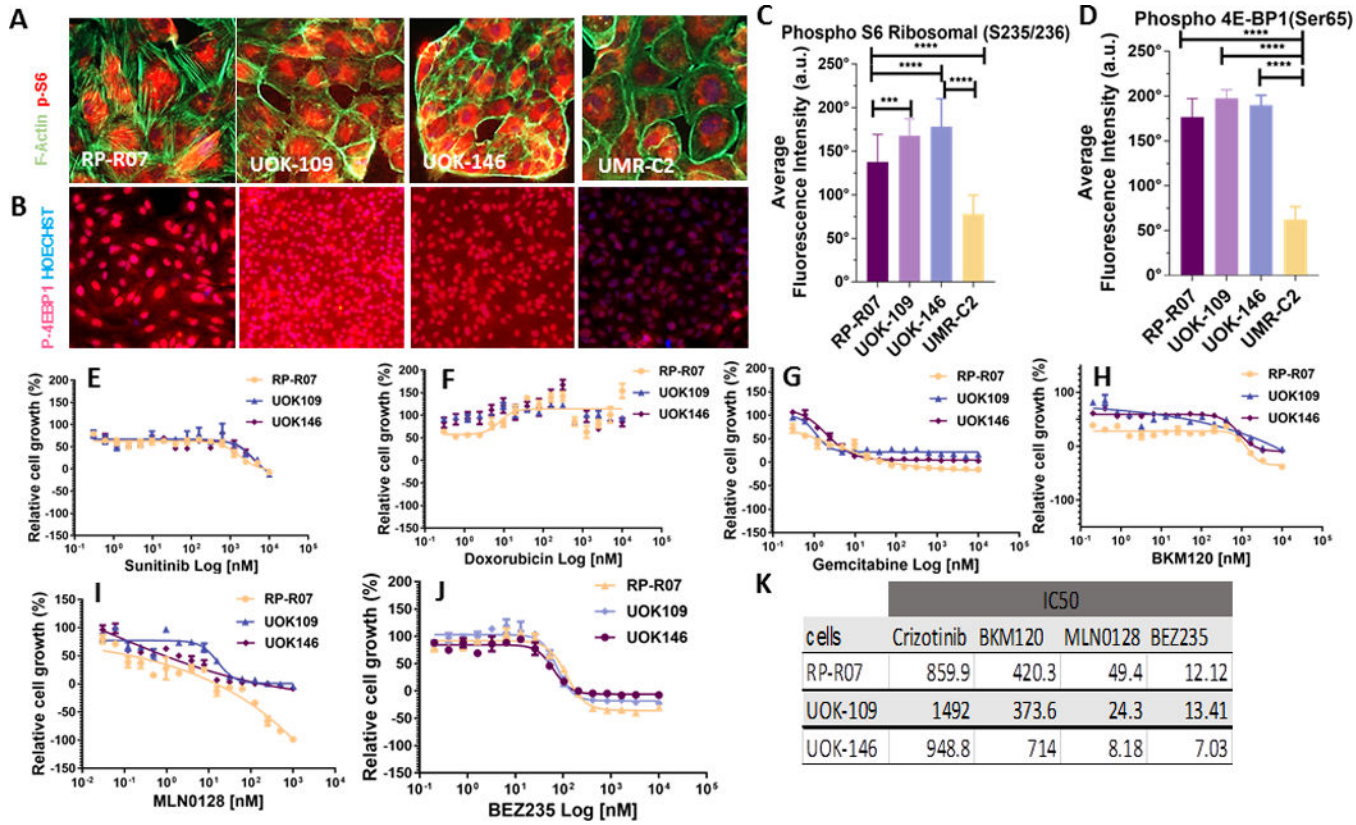

K

	IC50			
cells	Crizotinib	BKM120	MLN0128	BEZ235
RP-R07	859.9	420.3	49.4	12.12
UOK-109	1492	373.6	24.3	13.41
UOK-146	948.8	714	8.18	7.03

Figure 4. Simultaneous vertical inhibition of PI3K/AKT and mTOR pathways in tRCC.

A. PI3K/AKT/m-TOR pathway upregulation in tRCC. Representative immunofluorescence images of fixed tRCC cells; RP-R07, UOK-109, UOK-146 and ccRCC cell, UMR-C2, stained with: A. anti-phospho S6 (red) and anti F-actin (green), and Hoechst (blue); B. anti-phospho 4EBP-1 (red) and Hoechst (blue) and corresponding quantification (C, D). E-J. RP-R07 exhibits similar chemoresistance as observed in the patient. Three different tRCC cells, RP-R07, UOK-109, and UOK-146 were treated for 96 hours with indicated concentrations of different drugs. Cell growth was assessed by MTT assay and absorbance was measured at 589 nm. Each dot and error bar on the curves represents mean ± standard deviation (s.d.) (n = 8). All experiments were repeated at least three times. K. IC-50 Value of agent in H to J. BEZ-235 has the lowest IC-50 compared to other agents.

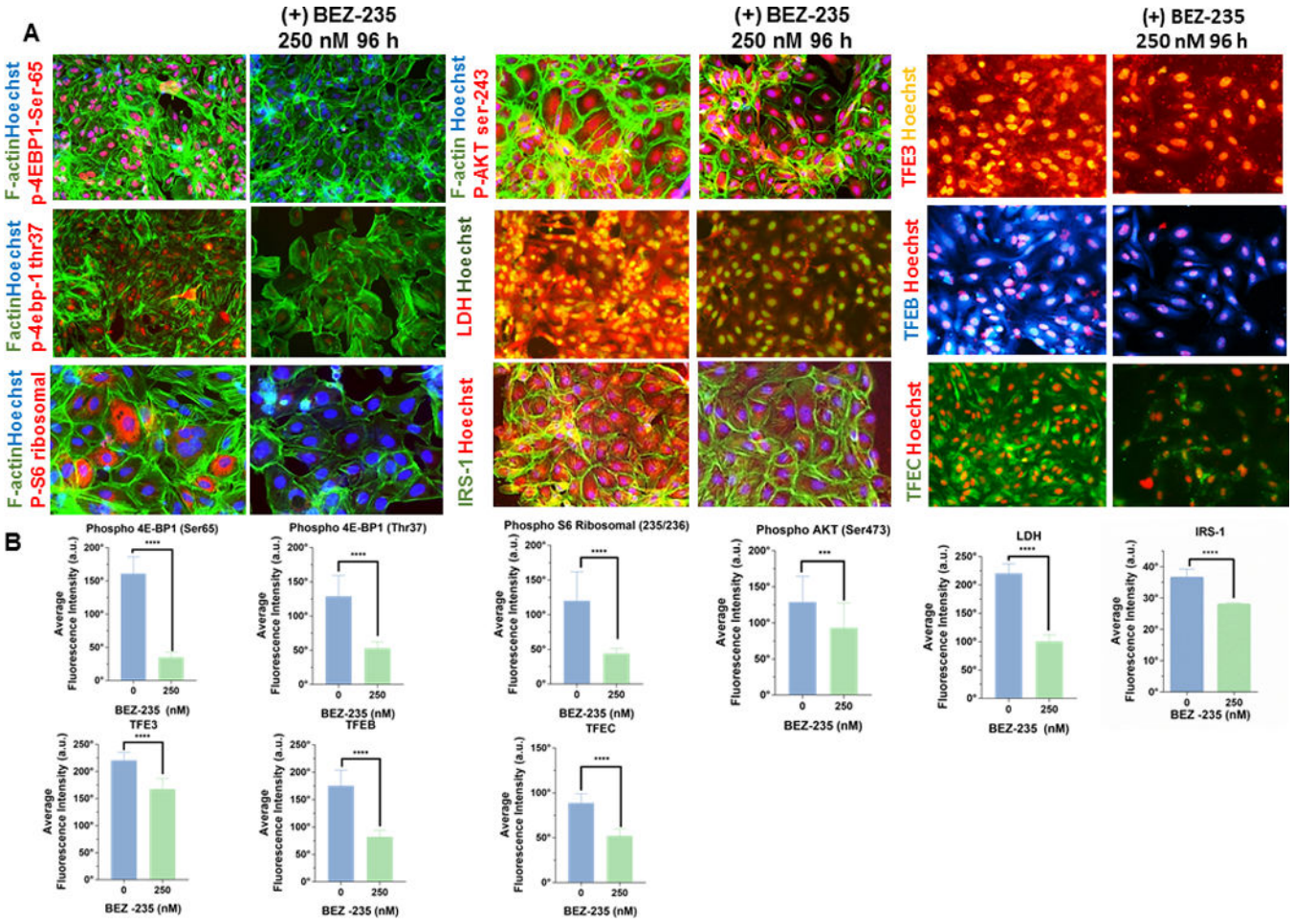

Figure 5. BEZ-235 treatment associates with attenuation of PI3K/AKT/mTOR pathway.

A. Immunofluorescence images of p-4EBP-1(ser 65), p-4EBP-1 (Thr37), pS6, p-AKT (S473), LDH, IRS-1, TFE3. TFEB, TFEC in BEZ-235 treated RP-R07 cells. B. Immunofluorescence quantification and student-t test analysis.

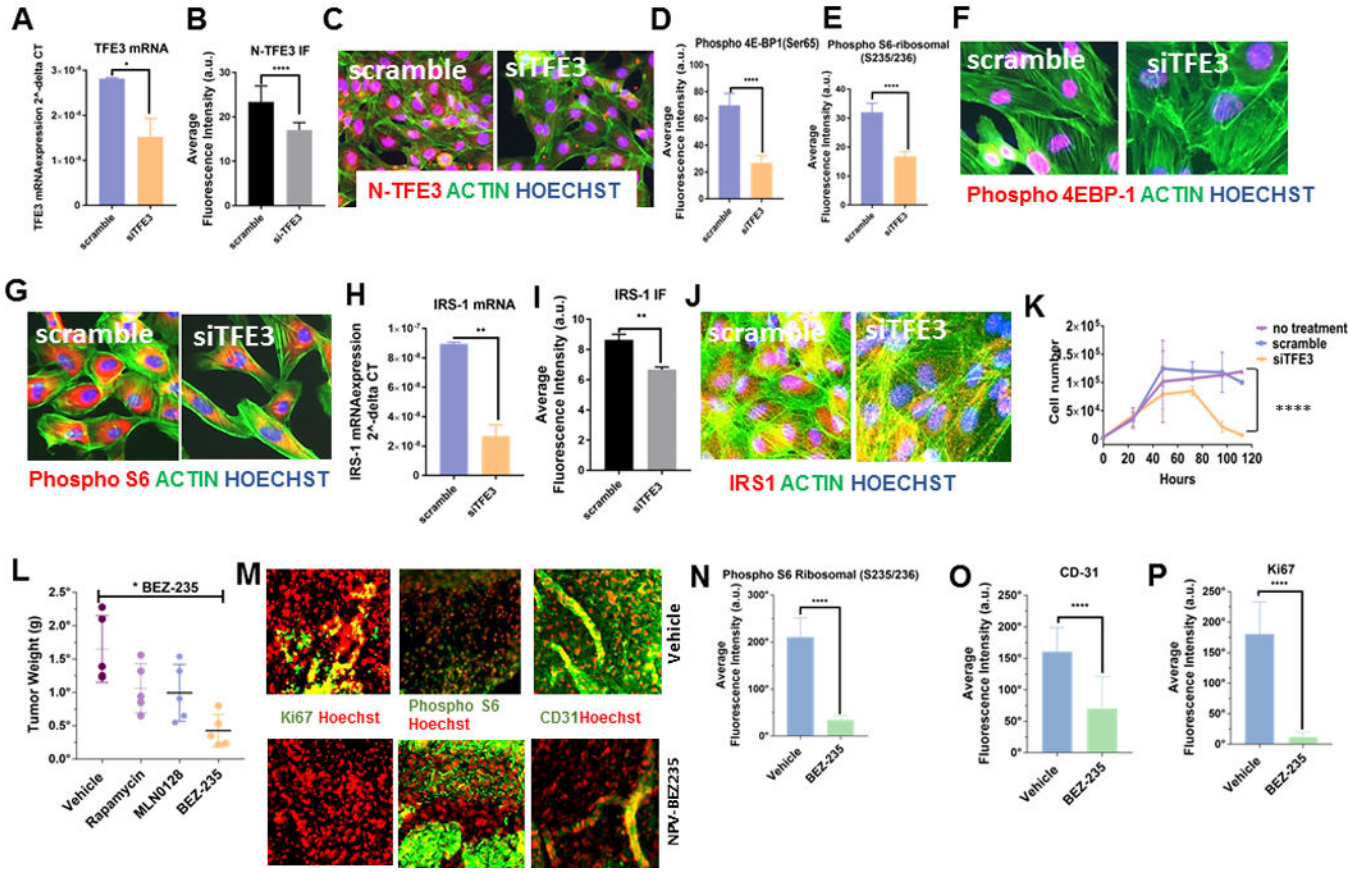

Figure 6. TFE3 transcriptionally regulates IRS-1, an upstream effector of PI3K/AKT/mTOR, and its downregulation inhibits RP-R07 cells proliferation.

°Evaluation of TFE3 knockdown by siRNA by qRT-PCR and by immunofluorescence. A. TFE3 mRNA expression level in RP-R07. B. Immunofluorescence quantification and student t-test analysis. C. Immunofluorescence images of N-terminal TFE3 in RP-R07. siRNA mediated silencing of TFE3 downregulates PI3K/AKT/mTOR downstream effectors 4EBP-1 (D, F) and S6 ribosomal (E, G) activity. Immunofluorescence quantification, student t-test analysis and representative immunofluorescence images. siRNA mediated silencing of TFE3 downregulates IRS-1 at the RNA-level (H) and protein level (I, J). Immunofluorescence quantification, student t-test analysis and representative immunofluorescence images. K. TFE3-siRNA inhibited RP-R07 cell proliferation. Graph represents cells number concentration (cells/mL) after treatment with no siRNA, siRNA control (scramble) and TFE3-siRNA (siTFE3) at 50 nM for 24 hours (siTFE3 *vs* scramble P= 0.74), 48 hours (siTFE3 *vs* scramble P= 0.38), 72 hours (siTFE3 *vs* scramble P= 0.13), 96 hours (siTFE3 *vs* scramble P= 0.04) and 110 hours (siTFE3 *vs* scramble P<0.0001). (L-P) Dual inhibition of PI3K-mTOR by BEZ-235 results in anti-tumor activity *in vivo*. RP-R07 cells (5×10^6) were injected subcutaneously into the flank of male SCID mice. Mice bearing RP-R07 xenograft tumors (n=5 for each group) were randomized into four groups (L 1. Vehicle 2. MLN0128 (3mg/kg) 3. Rapamycin (2 mg/kg) and 4. BEZ235 (25 mg/kg). No apparent drug toxicity was observed for each treatment. All mice were weighed twice weekly to monitor drug toxicities (i.e. ≥20% body weight loss). Dual inhibition PI3-mTOR

therapy significantly inhibits tumor growth. L. Average tumor weight (gram) in SCID mice treated with indicated single agent. Only tumors from mice treated with BEZ-235 was significantly smaller ($P<0.001$, One Way ANOVA, multiple comparison) than tumor from mice treated with vehicle. (M) Dual inhibition of PI3-mTOR by single agent BEZ-235 inhibits angiogenesis and attenuates PI3K-mTOR signaling *in-vivo.* Representative immunofluorescence images of paraffin embedded RP-R07 tumor slice (8 um) treated with vehicle (top) and BEZ-235 (bottom) stained with; anti Ki67 (left), anti-phosphoS6 ribosomal (middle), and angiogenesis marker CD31 (right). (N-P) Quantitative analyses.